Kirchhoff imaging beyond aliasing

Biondo L. Biondi

Stanford Exploration Project, Mitchell Bldg., Department of Geophysics,

Stanford University, Stanford, CA 94305-2215

(March 1, 2005)

ABSTRACT

Crucial image resolution may be lost when spatially aliased data are imaged with Kirchhoff algorithms that employ standard anti-aliasing methods. To maximize resolution, I introduce a method that enables the proper imaging of some aliased components in the data, while avoiding aliasing artifacts. The proposed method is based on a detailed analysis of the different types of aliasing that affect Kirchhoff imaging. In particular, it is based on the observation that operator aliasing depends on the dip-spectrum of the data. *A priori* knowledge on the characteristics of the dip-spectrum of the data, in particular on its asymmetry, can thus be exploited to enable "imaging beyond aliasing". The method is not of general applicability, but it successfully improves the image resolution when *a priori* assumptions on the data dips are realistic. The imaging of salt-dome flanks in the Gulf of Mexico has been enhanced by the application of the proposed method.

INTRODUCTION

High resolution is a paramount goal of seismic imaging. Unfortunately, we often face a trade-off between resolution and the signal-to-noise ratio because of incomplete spatial sampling of the data. To sample the data adequately is expensive, and in many cases outright impossible. Too often the data are not adequately sampled and cannot be imaged with maximum resolution by standard imaging methods. In order to avoid aliasing noise, standard imaging methods discard some of the high-frequency components of the signal that have been recorded. In this process valuable image resolution is lost.

Imaging beyond aliasing is therefore a very active area of research. A promising direction aims to exploit the redundancy of multi-offset data sets and generate alias-free and high-resolution stacks (Brink et al., 1997) or partial stacks (Chemingui and Biondi, 1998). However, these methods are based on the inversion of prestack imaging operators [Dip Moveout (DMO) (Ronen, 1987) or Azimuth Moveout (AMO) (Biondi et al., 1998)] that are computationally demanding. Another approach based on inversion, but less computationally demanding, is the interpolation of aliased data by prediction-error filters (Claerbout, 1997; Cary and Goodway, 1997; Crawley, 1998). Wisecup (1998) presented an interesting method to exploit data redundancy over offset to overcome temporal aliasing. Cary (1997) successfully applied this idea to overcome spatial aliasing during the stacking process. The application of Wisecup's idea to overcome spatial aliasing during migration certainly has potential, but has not been developed yet. Huygens migration methods (Neidell, 1997) are also promising, and have been shown to yield high-resolution results, although their theoretical foundations need to be further developed.

The goal of the anti-aliasing method presented in this paper is to improve the image resolution by properly imaging some of the aliased components of the recorded data, that would not be imaged

by the application of standard anti-aliasing methods of Kirchhoff operators (Gray, 1992; Bevc and Claerbout, 1992; Lumley et al., 1994; Abma et al., 1998). My goal is thus more modest than the ones of the research discussed above, but the proposed method has the advantage of not requiring complex, and sometime unreliable, inversion techniques. In addition, it does not require data redundancy, and thus can be applied to the imaging of minimal data sets (Padhi and Holley, 1997), such as zero-offset data.

I show that when a simple modification of the anti-aliasing conditions of the Kirchhoff migration operator is made, some of the aliased components in the data are nicely imaged, without the generation of aliasing noise. This "imaging beyond aliasing" is made possible by the exploitation of *a priori* assumptions on the dip bandwidth of the data. These assumptions are realistic in many important cases, such as the example that I show of the imaging of the steep flanks of a salt dome in the Gulf of Mexico. Pica (1996) presented a model-based anti-aliasing method that is related to the one presented in this paper. However, his analysis is based on *a priori* information on the image dips instead of on data dips, and it yields different anti-aliasing conditions.

To derive the proposed anti-aliasing method, I analyze in detail the aliasing of Kirchhoff imaging operators, and how imaging-operator aliasing interacts with simple data aliasing. I distinguish two types of imaging-operator aliasing: image-space aliasing and data-space aliasing. Image aliasing occurs when the imaging operator, represented by its spreading formulation (e.g., ellipsoid for migration) is too coarsely sampled in image space. Dually, data-space aliasing occurs when the gathering formulation of the imaging operator (e.g., hyperboloid for migration) is too sparsely sampled. Data-space aliasing is often referred simply as "operator aliasing" in the literature; in the following I will follow this convention.

Operator aliasing may occur even when the data are are not aliased. However, I demonstrate

that when the data are not aliased, and the data sampling is the same as the image sampling, image aliasing is closely related to operator aliasing. In this cases, the "conventional" conditions necessary to avoid operator aliasing (Gray, 1992; Bevc and Claerbout, 1992; Lumley et al., 1994; Abma et al., 1998) guarantee also an image free of aliasing, and vice versa. Therefore, the two concepts are seldom distinguished and often only the conditions necessary to avoid operator aliasing are used to avoid aliasing artifacts or, more rarely, only the conditions necessary to avoid image aliasing are used (Hale, 1991). The distinction between image aliasing and operator aliasing becomes important when the above conditions are not fulfilled. In this paper I focus on the situations when the data are aliased but *a priori* knowledge of their dip spectrum can be exploited to obtain higher-resolution images than possible with conventional methods. The distinction is also important when imaging prestack data sets that have larger dimensionality, and consequently a different sampling, than the image.

The anti-aliasing theory presented in this paper is strictly valid only when the summation surfaces of the Kirchhoff operator are planar. In most of the practical cases the curvature of the imaging operator is sufficiently small that the errors introduced by neglecting it are also small. Wave-equation datuming and AMO are two seimic operators that may present strong curvature. Druzihinin (1999) presents a general anti-aliasing method based on numerical-quadrature theory that addresses the problem for wave-equation datuming. Biondi et al. (1998) solve the problem for AMO by transforming the integration variables to assure that the operator curvature is well behaved.

THE ANTI-ALIASING DILEMMA

In Kirchhoff imaging, operator aliasing is usually avoided by the suppression of some high-frequency components during the summation process. Unfortunately, this lowpass filtering decreases the image resolution when the data are aliased. We therefore face a dilemma when imaging aliased data: on one

side, to avoid aliasing noise we need to apply anti-aliasing filters, on the other side, we do not want to lose image resolution. Figure 1 exemplifies the problem. It shows the results of 3-D zero-offset time migration of a salt-dome flank in the Gulf of Mexico. The section on the left (Figure 1a) was 3-D migrated without the use of any anti-aliasing filter, while the section on the right (Figure 1b) was obtained with a standard anti-aliased migration. Whereas the image obtained without anti-aliasing is much noisier than the anti-aliased one, it also has higher resolution. In the shallow part of the section shown in Figure 1a, the aliasing noise is so strong that it is impossible to appreciate the higher resolution of Figure 1a compared with Figure 1b. But when zooms into the deeper part of the sections are compared (Figure 2), it is apparent that we lose resolution by applying anti-aliasing. In particular, the high-frequency dipping event at about CMP X=700 m and Time=2.2 s is poorly resolved in the anti-aliased migration (Figure 2b). The anti-aliased migration misses a whole wavelet cycle of the sediment truncation against the salt flank. If we consider that hydrocarbon reservoirs are often located at the sediment-salt interfaces, we appreciate the potential advantages of improving the resolution of such events.

In this example, migration without anti-aliasing achieves higher resolution than anti-aliased migration because it images data components that are aliased in the data space. In particular, the steeply dipping energy reflected from the salt flanks visible in the data window shown in Figure 3 are aliased. Figure 4 shows the frequency-wavenumber spectrum of the data window in Figure 3. Figure 4 shows the central band of the spectrum and its two replicas on either side. The vertical white lines correspond to the Nyquist wavenumbers. The two "replicated bands" are caused by the spatial discretization, and their existence is at the root of the aliasing problem. The dipping events that appear aliased in the data window correspond to the "clouds" in the spectrum contoured with ellipses in Figure 4. The ellipse marked as **B** contours the energy that can be correctly migrated. The cloud starts in the main band but crosses the positive Nyquist line and trespasses upon the replicated band on the positive

side. The portion of the cloud that crosses the positive Nyquist corresponds to the signal components that are lost when conventional anti-aliased migration is applied (Figures 1b and 2b), and that are responsible for the high resolution achieved by migration without anti aliasing (Figures 1a and 2a). Because there are no events dipping with negative time dips, the simple anti-aliasing method presented in this paper enables both the imaging of the high-frequency components and the suppression of aliasing noise. The ellipse marked as **A** contours the energy that cannot be correctly migrated and should be avoided during the summation.

ALIASING IN IMAGE SPACE

The simplest type of aliasing related to the imaging operator is **image-space aliasing**. It occurs when the spatial sampling of the image is too coarse to represent adequately the steeply dipping reflectors that the imaging operator attempts to build during the imaging process. In other words, image-space aliasing is caused by excessively coarse sampling of the image space, with consequent aliasing of the migration ellipsoid. With Kirchhoff imaging the choice of image sampling is arbitrary, and thus image aliasing can be simply avoided by increasing the density of the image. However, the cost of migration grows proportionally with image density. For a given spatial sampling of the image, to avoid image aliasing we need to limit during the migration the frequency content of the image as a function of reflectors' dips. This goal can be accomplished by the application of a dip-dependent temporal lowpass filtering of the input data during the summation process.

An efficient method to lowpass filter time-domain data with variable frequency is the triangle-filters method described in *Basic Earth Imaging* (Claerbout, 1995). An alternative method is to precompute lowpassed versions of the input traces, and select the appropriate input data during summation (Gray, 1992). This second method is potentially more accurate than triangle filtering, and it is

more computationally efficient when each input trace is summed into many output traces, as happens for 3-D migrations (Abma et al., 1998). However, this method may require storing many versions of the input data. To reduce the storage requirements without affecting the accuracy I linearly interpolate the lowpassed traces along the frequency axis during the summation.

The anti-aliasing constraints used to avoid image aliasing can be easily derived from basic sampling theory. For the case of time migration, when the coordinates of the image space are $\vec{\mathbf{I}} = (\tau_I, x_I, y_I)$, the pseudo-depth frequency f_τ^I must fulfill the following inequalities:

$$\begin{aligned} f_\tau^I &< \frac{1}{2\Delta x_I \left| p_x^{\mathrm{I}} \right|}, \\ f_\tau^I &< \frac{1}{2\Delta y_I \left| p_y^{\mathrm{I}} \right|}; \end{aligned} \tag{1}$$

where Δx_I and Δy_I are respectively the image sampling rate of the x_I and y_I axes, and p_x^{I} and p_y^{I}, are the operators' dips in image space.

As discussed above, it is convenient to apply an anti-aliasing filter as a band-pass filter of the input traces, before their contributions are summed into the output image. Therefore, we need to recast the constraints on the pseudo-depth frequency f_τ^I of equations (1) into constraints on the input data frequency f_t^D. This distinction is important because the frequency content of the seismic wavelet changes during the imaging process because of stretching, or compression, of the time axis. In particular, during time migration the wavelet is always stretched; neglecting this stretch would lead to anti-aliasing constraints that are too stringent. Notice that the seismic wavelet may get compressed, instead of stretched, by other imaging operators, such as inverse DMO and AMO (Biondi et al., 1998). The pseudo-depth frequency of the image and the temporal frequency of the data are thus linked by the **wavelet-stretch factor** $dt_D/d\tau_I$, as $f_\tau^I = f_t^D dt_D/d\tau_I$, where t_D is the time coordinate in the data space. Taking into account the wavelet-stretch factor, we can write the constraints on the data frequency that control image aliasing, as a function of the image sampling rates Δx_I and Δy_I, the

image dips p_x^{I} and p_y^{I}, and the wavelet-stretch factor $dt_D/d\tau_I$,

$$\begin{aligned} f_t^D &< \frac{1}{2\Delta x_I \left| p_x^{\mathrm{I}} \right| \frac{dt_D}{d\tau_I}}, \\ f_t^D &< \frac{1}{2\Delta y_I \left| p_y^{\mathrm{I}} \right| \frac{dt_D}{d\tau_I}}. \end{aligned} \tag{2}$$

Image anti-aliasing for 3-D prestack time migration

For 3-D prestack time migration, the reflectors dips p_x^{I} and p_y^{I}, and the wavelet-stretch factor $dt_D/d\tau_I$, can be analytically derived as functions of the input and output trace geometry and the input time. Appendix A presents the derivation of these analytical relationships, which I use for the following examples.

To gain intuition about the effects of incorporating an anti-aliasing filter in a migration operator, it is instructive to analyze the images generated when one single input trace is migrated into a cube. Figure 5 shows the result produced when one trace is migrated without the application of any anti-aliasing filter. The input trace was recorded at an offset of 2.4 km and the velocity was assumed to be constant and equal to 1.5 km/s. The image sampling was 20 m in each direction ($\Delta x_I = \Delta y_I = 20$m). Strong aliasing artifacts are visible in both the time slices and the vertical section.

Figure 6 shows the result produced when the same data trace is migrated with an appropriate anti-aliased operator. Notice that the aliasing artifacts disappear as the frequency content of the imaged reflectors progressively decreases, as the dips increase. Figure 7 shows the result of migrating the same data trace when the effects of the wavelet stretch are not taken into account; that is, by setting $dt_D/d\tau_I = 1$. In this case, the anti-aliasing filter over-compensates for the image dip and valuable resolution is lost at steep dips. Examining the time slice shown on the top of Figure 7, we notice that the loss of resolution is larger for regions of the migration ellipses with a steep dip along the cross-line direction.

Figure 8 shows the effects of image-space aliasing on the migrated results from the salt-dome data set shown in Figure 1. Figure 8a shows the migration results obtained without the use of any anti-aliasing and with $\Delta x_I = 36$ m; that is the original sampling of the zero-offset data. Shallow dipping reflectors and the steep high-frequency event at about 2.2 s are badly aliased. The quality of the image improves when the image spatial sampling is halved to $\Delta x_I = 18$ m (Figure 8b). It is useful to notice that the traces in Figure 8a are exactly the same as the odd traces in Figure 8b. Therefore, image aliasing does not add noise to the image, it just makes the interpretation of the image more difficult and ambiguous. The application of the image-space anti-aliasing constraints, expressed in equation (2), further improves the image quality, in particular for the shallower events (Figure 8c). Although the image in Figure 8c is less noisy than the images in Figures 8a and 8b, it is still contaminated by aliasing artifacts. These artifacts are caused by **operator aliasing**, or data-space aliasing. The next section analyzes the causes of operator aliasing, and presents anti-aliasing constraints used to eliminate it.

OPERATOR ALIASING

The previous section analyzed aliasing in the image space, which occurs when the spreading representation of the imaging operator is aliased. Data-space aliasing, the dual of image-space aliasing, occurs when the gathering representation of the imaging operator is aliased in the data space. This data-space aliasing is commonly called **operator aliasing**. Operator aliasing is different than data aliasing, and it may occur even when the data are sufficiently sampled. When operator aliasing occurs, noise is actually added to the image, in contrast to the image-space aliasing case when the interpretability of the image is hampered by missing data, not additive noise. To illustrate the issues related to operator aliasing, the next set of figures analyze a simple example in which the data are plane waves and the summation operator is a slant stack.

Figures 9 and 10 show two plane waves. The plane waves are adequately sampled when the waveform is a 30 Hz sinusoid (Figure 9a), but the one with positive time dip is aliased when the waveform is a 60 Hz sinusoid (Figure 10a). The data aliasing is obvious in the time-space domain, where the data appears to be dipping in the opposite direction.

Data summation along a given trajectory is equivalent to a two-step process; first, the data are shifted so that the events align along the desired trajectory. Second, the traces are stacked together. In the case of the slant-stack operator, the summation trajectories are lines and the first step is equivalent to the application of linear moveout (LMO) with the desired dip. Figures 9b and 10b show the results of applying LMO with the slowness of the positive-dip plane wave to the data respectively in Figures 9a and 10a. Figures 9c and 10c show the results of applying LMO with the slowness of the negative-dip plane wave to the data respectively in Figures 9a and 10a. The traces on the right side of the sections are the results of stacking the corresponding data, each plane wave independently. The solid line is the stack of the positive-dip plane wave, and the dotted line is the stack of the negative-dip plane wave. At 30 Hz no aliasing occurs and only the desired plane wave stacks coherently after applying LMO with either slowness. In contrast, at 60 Hz both plane waves stack coherently after applying LMO with either slowness (Figures 10b and 10c). In general, artifacts are generated when data that are not aligned with the summation path stack coherently into the image. This phenomenon is the cause of the **aliasing noise** that degrades the image when operator aliasing occurs.

To avoid adding aliasing noise to the image, we could lowpass-filter the input data according to the operator dips. A reasonable strategy is to limit the migration operator to the data components in the main band of the data spectrum (e.g. between the negative Nyquist and the positive Nyquist lines in the spectrum shown in Figure 4). This strategy leads to the application of the following

anti-aliasing constraints on the temporal frequency of the summation operator:

$$\begin{aligned} f_t^D &< \frac{1}{2\Delta x_D \left| p_x^{\mathrm{D}} \right|}, \\ f_t^D &< \frac{1}{2\Delta y_D \left| p_y^{\mathrm{D}} \right|}; \end{aligned} \tag{3}$$

where Δx_D and Δy_D are the sampling rates of the data axes, and p_x^{D} and p_y^{D} are the operator dips in the data space, that is, the dips of the summation operator (i.e hyperboloid for migration). These, or equivalent, relationships have been presented by a number of authors (Gray, 1992; Bevc and Claerbout, 1992; Lumley et al., 1994; Abma et al., 1998).

The application of these constraints to the simple slant stack example of Figures 9 and 10 (Δx_D=25 m, p_+^{D}=.5 s/km, p_-^{D}=-.166 s/km) would result in the suppression of all the frequencies above 40 Hz when summing along the positive dip and the suppression of all the frequencies above 120 Hz when summing along the negative dip. At 60 Hz, both the signal and the operator aliasing noise would be suppressed when summing along the positive dip (p_+^{D}=.5 s/km), but both would be preserved when summing along the negative dip (p_-^{D}=-.166 s/km). The outcome of applying the "standard" anti-aliasing criteria is thus sub-optimal.

To examine further the relationship between operator aliasing and the dip bandwidth in the data, we consider the two plane waves shown in Figure 11. In this case the two plane waves have a 60 Hz waveform, as in Figure 10, but the second plane wave is dipping less than in the previous case (p_-^{D}=-.025 s/km). The two plane waves have conflicting dips, but even at 60 Hz they do not interfere with each other during summation because the difference between the conflicting dips is smaller. However, the anti-aliasing conditions expressed in equation (3) would apply exactly in the same way as in the previous case. Their application would cause the suppression of the signal when summing along the positive dip, even if the stack is free of operator aliasing noise.

The previous examples show that the anti-aliasing conditions expressed in equation (3) can be

either too restrictive or too lax. Although these conditions may be correct for several important cases, they do not take into account the fact that operator aliasing depends on the presence of conflicting, and potentially aliased, dips in the data. They implicitly assume that no dips are aliased in the data. When this implicit assumption is violated, as for the positive dip in the previous example, it can be harmful to apply the "standard" anti-aliasing conditions, and we need to introduce new anti-aliasing conditions. To derive more general anti-aliasing conditions we need to take into account the existence of conflicting dips, and the phenomenon of spectral replication caused by discretization, as exemplified in Figure 4.

Figure 12 graphically shows the idea at the basis of the new anti-aliasing criteria introduced in this paper. The shaded area is the widest possible area of the spectrum where there is no interference with aliased energy; that is, the data components in the shaded areas can be safely imaged without generating operator-aliasing noise. The boundaries of this "pass region" are determined as a function of the minimum data dips, $\mathbf{p}^{\min} = \left(p_x^{\min}, p_y^{\min}\right)$, and maximum data dips, $\mathbf{p}^{\max} = \left(p_x^{\max}, p_y^{\max}\right)$. On the negative wavenumber side the pass region is bound by a line representing a replica of the maximum dip line. That is, by a line that starts at -2k_{Nyq} (where k_{Nyq} is the Nyquist wavenumber) and has a slope corresponding to the maximum dip. Similarly, on the positive wavenumber side the pass region is bound by a line starting at 2k_{Nyq} and with slope corresponding to the minimum dip.

The boundaries for the pass region are analytically expressed by the following inequalities:

$$p_x^{\max} - \frac{1}{f_t^D \Delta x_D} < p_x^{\mathrm{D}} < p_x^{\min} + \frac{1}{f_t^D \Delta x_D}, \tag{4}$$

$$p_y^{\max} - \frac{1}{f_t^D \Delta y_D} < p_y^{\mathrm{D}} < p_y^{\min} + \frac{1}{f_t^D \Delta y_D}. \tag{5}$$

The inequalities expressed in equations (4-5) can be easily recast as anti-aliasing constraints on the maximum frequency in the data, as

$$f_t^D < \frac{1}{\Delta x_D \left(p_x^{\mathrm{D}} - p_x^{\min}\right)}, \tag{6}$$

$$f_t^D < \frac{1}{\Delta x_D \left(p_x^{\max} - p_x^{\mathrm{D}}\right)}, \tag{7}$$

$$f_t^D < \frac{1}{\Delta y_D \left(p_y^{\mathrm{D}} - p_y^{\min}\right)}, \tag{8}$$

$$f_t^D < \frac{1}{\Delta y_D \left(p_y^{\max} - p_y^{\mathrm{D}}\right)}. \tag{9}$$

The constraints expressed in equations (6–9) can be used as alternatives, or, in conjunction with the constraints expressed in equation (3), to design anti-alias summation operators.

Comparing equation (3) with equations (6–9), we can notice that the two sets of constraints are equivalent when, for each frequency, the data dip limits $p^{\min}$ and $p^{\max}$ are respectively set to $-k_{\mathrm{Nyq}}/2\pi f_t^D$ and $k_{\mathrm{Nyq}}/2\pi f_t^D$, as it is easy to verify by substituting $p_x^{\min} = -1/2\Delta x_D f_t^D$ into equation (6), and $p_x^{\max} = 1/2\Delta x_D f_t^D$ into equation (7). This implies that when we can assume that there is no spatial aliasing in the data, the new anti-aliasing conditions are equivalent to the "standard" conditions.

Applying the constraints of equations (6–9) to the plane-waves examples of Figures 9–11 lead to the "correct" choice of frequency cutoffs. In the case with wide dip bandwidth (Figures 9–10; p_+^{D}=.5 s/km, p_-^{D}=-.166 s/km) the frequency cutoff is 60 Hz when summing along both the positive and the negative dips. The plane waves in Figure 10 are thus just outside the pass region and should be suppressed. In the case with narrow dip bandwidth (Figure 11; p_+^{D}=.5 s/km, p_-^{D}=-.025 s/km) the frequency cutoff is about 84 Hz when summing along both the positive and the negative dips. Therefore, both plane waves in Figure 10 can be safely imaged.

The data-dips' limits, $\mathbf{p}^{\min}$ and $\mathbf{p}^{\max}$, can vary in both time and space, according to the local dips in the data. Therefore, the anti-aliasing filtering applied to the data as a consequence of the constraints in equations (6–9) can be fairly complex, and dependent on factors including local dips, time, and spatial coordinates. If no *a priori* knowledge of the local dips is available, and the summation is carried out along the midpoint axes, twice the inverse of propagation velocity is a reasonable bound

on the absolute values of both $\mathbf{p}^{\min}$ and $\mathbf{p}^{\max}$. In contrast, in the case that the summation is performed along the offset axes, as for CMP stacks, $\mathbf{p}^{\min}$ can be safely assumed to be positive, and at worst equal to zero. Therefore, imaging operators that sum data over the offset axes, such as NMO followed by stack, are less prone to spatial aliasing than imaging operators that sum data over midpoints, such as migration.

The most substantial benefits of applying the more general constraints expressed in equations (6–9) are achieved when asymmetric bounds on the dips in the data enable imaging the high-frequency components that are present in the data as aliased energy, without creating aliasing artifacts. These components would be filtered out if the constraints in equation (3) were applied. Asymmetric bounds on the data dips are realistic in the important application of imaging steep salt-dome flanks, as in the Gulf of Mexico data set shown above. In this case, we can assume that the negative time dips in the data are small. According to equations (4-5), the increase in $p^{\min}$, i.e. the decrease of its absolute value, increases the maximum positive dip that can be imaged without operator aliasing. In practice, the application of the generalized constraints in equations (6–9), with $\mathbf{p}^{\min} \neq \mathbf{p}^{\max}$, causes the migration operator to be asymmetric, with dip bandwidth dependent on reflector direction.

Figures 13 and 14 show an example of the effects of asymmetric dip bounds on the migration operator. For both images, the image sampling is the same as in Figure 6 ($\Delta x_I = \Delta y_I = 20$m), but the data sampling is assumed to be coarser than the image sampling by a factor of two; that is, $\Delta x_D = \Delta y_D = 40$m. When the constraints in equation (3) are applied (see Figure 13), the operator has lower resolution than in Figure 6. But if we assume that $p_x^{\min} = 0$ s/m, and apply the constraints in equations (6–9) the pass region for the operator is augmented by the band comprised between k_{Nyq} and $2k_{\text{Nyq}}$ (see Figure 12). Consequently, in Figure 14 the positive time dips are imaged with the same resolution as in Figure 6.

The link between operator anti-aliasing and image anti-aliasing

The constraints derived to avoid operator aliasing and image aliasing are different in general; both sets of constraints must be respected if a high-quality image is to be assured. However, the two sets of constraints are equivalent in many practical situations. In these situations only one set of constraints need to be applied to assure that the image is both adequately sampled and free of operator-aliasing noise. The analysis is simple for time migration of zero-offset or constant-offset data, where we can assume that the summation surfaces $t_D = t_D(\vec{\mathbf{I}}, x_m, y_m)$ are only functions of the relative distance between the image-point $\vec{\mathbf{I}}$ and the midpoint of the data trace (x_m, y_m).

The first condition for linking image aliasing to operator aliasing is that the data are not spatially aliased, and thus the operator anti-aliasing constraints expressed in equation (3) are equivalent to the constraints expressed in equations (6–9). Comparing the constraints for operator anti-aliasing [equation (3)] with the constraints for image anti-aliasing [equation (2)], we can easily notice that a necessary condition for their being uniformly equivalent is that the data sampling rates Δx_D and Δy_D be equal to the image sampling rates Δx_I and Δy_I.

The other necessary conditions are that $p_x^{\mathrm{D}} = p_x^{\mathrm{I}} dt_D/d\tau_I$ and $p_y^{\mathrm{D}} = p_y^{\mathrm{I}} dt_D/d\tau_I$; that is, that the ratio between the operator dips in the data space and the operator dips in the image space are exactly equal to the wavelet-stretch factor discussed in the section on image aliasing. These conditions are fulfilled in the important case of spatially invariant imaging operators, as it can be shown by applying the chain rule to the derivative of the summation surfaces $t_D = t_D(\vec{\mathbf{I}}, x_m, y_m)$ with respect to the midpoint coordinates of the data trace (x_m, y_m):

$$\begin{aligned} p_x^{\mathrm{D}} = \frac{dt_D}{dx_m} &= \frac{dt_D}{d\tau_I}\frac{d\tau_I}{dx_I}\frac{dx_I}{dx_m} = \frac{dt_D}{d\tau_I} p_x^{\mathrm{I}} \\ p_y^{\mathrm{D}} = \frac{dt_D}{dy_m} &= \frac{dt_D}{d\tau_I}\frac{d\tau_I}{dy_I}\frac{dy_I}{dy_m} = \frac{dt_D}{d\tau_I} p_y^{\mathrm{I}}. \end{aligned} \tag{10}$$

The equalities in (10) rely on the horizontal invariance of the imaging operator; they require that

the derivatives of the horizontal coordinates of the image point with respect to the horizontal coordinates of the data trace (dx_I/dx_m and dy_I/dy_m) be equal to one. For migration, these conditions are strictly fulfilled only in horizontally layered media, though they are approximately fulfilled when migration velocity varies smoothly. Another way to interpret this result is to recall that migration in the frequency-wavenumber domain is equivalent to a down-shift in temporal frequency at constant wavenumber (Stolt, 1978); that is, if both the data and the operator are not aliased, the image is guaranteed to be not aliased. Because the equalities in (10) do not require any other assumptions on the shape of the summation surfaces, the same link between operator aliasing and image aliasing exists for all spatially-invariant integral operators, such as DMO (Hale, 1991) and AMO (Biondi et al., 1998).

The distinction between operator aliasing and image aliasing can thus be safely ignored when well sampled zero-offset data are *time* migrated (Bevc and Claerbout, 1992; Lumley et al., 1994; Claerbout, 1995), and only one set of constraints between equation (3) and equation (2) must be applied, but it ought to be respected when irregularly sampled prestack data are *depth* migrated. The distinction is also important when *a priori* assumptions on the dips in the data permit less stringent operator anti-aliasing constraints to be set, so that reflectors can be imaged with high resolution but without operator-aliasing artifacts. In these cases it is important to use a finer spatial sampling for the image than for the data to avoid aliasing the image. The next section shows an example of this situation.

An open, and more subtle, question remains regarding the operator aliasing of prestack data, that in general do not constitute a minimal data set (Padhi and Holley, 1997). However, even in this case, the constraints to avoid image aliasing [equation (2)] must be respected for the production of high-quality and interpretable images.

HIGH-RESOLUTION IMAGING OF SALT FLANKS

The high-resolution imaging of salt-dome flanks is an important application of the theory described in the previous two sections. In this case, we can often assume that in the proximity of the salt flanks, the data contains no, or little, energy dipping in the direction opposite to the reflections from the flanks. According to the theory developed in the previous section, this assumption enables the salt flanks to be imaged with higher resolution than was otherwise possible. However, it is important to be aware that when the image frequency content is increased by the application of the constraints in equations (6–9), in place of the constraints in equation (3), we run the risk of aliasing the image. As discussed in the previous section, the conditions that avoid operator aliasing do not guarantee the avoidance of image aliasing. Therefore, the constraints to avoid image aliasing [equation (2)] must also be taken into account, and the image sampling must be reduced so that both goals, of avoiding image aliasing and preserving high-frequency components, can be achieved. Because of image-aliasing considerations, the images of the salt flanks from the Gulf of Mexico data that are shown in the following figures are sampled twice as densely ($\Delta x_I = \Delta y_I = 18$m) as the zero-offset data ($\Delta x_D = \Delta y_D = 36$m).

To apply the high-resolution imaging method presented in this paper, the first step is to determine the appropriate values for the bounds on the data dips. For the sake of simplicity, for this example I choose constant bounds; that is, $p_x^{\min} = -.082$ s/km, $p_x^{\max} = .48$ s/km, $p_y^{\min} = -.8$ s/km, $p_y^{\max} = .8$ s/km. In more geologically complex cases, it may be advantageous to allow the data-dip bounds to vary both in time and space. Figure 15 shows the same data spectrum as Figure 4; the dashed lines superimposed onto the spectrum cover the areas determined by the inequalities of equations (4-5) (and graphically shown in Figure 12), according to the chosen bounds for $p_x^{\min}$ and $p_y^{\max}$. The area that honor all anti-aliasing constraints, and that thus represents data components used by the imaging,

is covered by both sets of crossing dashed lines. A large swath of the aliased energy with positive time dips is used by the high-resolution imaging, whereas it would be discarded if standard anti-aliasing methods were used.

The improvements in image resolution that are made possible by the proposed anti-aliasing method are demonstrated in Figures 16–18. Figure 16a shows the results of 3-D post-stack migration obtained without any anti-aliasing. Figure 16b shows the results obtained when the new anti-aliasing constraints in equations (6–9) are applied. Figure 16c shows the results produced when the standard anti-aliasing constraints in equation (3) are applied. The differences between the results are better appreciated by a comparison of windows zooming into smaller parts of the sections. Figure 17 shows the comparison for the shallower part of the section. The image obtained without anti-aliasing is uninterpretable because of the strong aliasing noise. The image obtained with the proposed method shows better resolution of several dipping reflectors and of the steep salt flank. Figure 18 demonstrates (for the same area shown in Figure 2) that the high-frequency sediment truncation against the salt flank (CMP X=700 m and Time=2.2 s), is well resolved in the image obtained with the proposed method, whereas it is poorly resolved in the image obtained with traditional methods.

Notice that the images obtained with the proposed method show still lower resolution than the images obtained without anti-aliasing. Higher resolution could have been achieved if I had set $p_x^{\min}$ to an even higher value. However, operator aliasing noise would have begun to creep into the image. For example, if in Figure 15 I had set $p_x^{\min} = 0$ s/km instead of $p_x^{\min} = -.082$ s/km, the line bounding the pass region on the positive side would have become vertical. The pass region would have included more of the signal corresponding to the salt flanks, but also the alias corresponding to the flat sediments. A careful examination of Figure 15 also shows that when I chose the value of $p_x^{\max}$ to be equal to .48 s/km I included in the pass region some aliased components of the salt-flank reflections in order to preserve the resolution of the flat sediments.

CONCLUSIONS

When imaging data affected by spatial aliasing, we would like not to be forced to trade off resolution for signal-to-noise ratio, but, unfortunately the application of conventional anti-aliasing criteria yields poorly resolved images. A more comprehensive understanding of aliasing of Kirchhoff-like imaging operators leads to the derivation of new anti-aliasing criteria, that can be used when *a priori* knowledge of the structure in the target zone enables us to make realistic assumptions on the dip content of the data. The application of these anti-aliasing criteria yields images with higher resolution than the images obtained by applying the standard anti-aliasing criteria. The example also demonstrates that the fundamental trade-off between resolution and the signal-to-noise ratio still persist even when applying the proposed anti-aliasing criteria, though at a more satisfactory level.

Imaging of steeply dipping salt flanks is an important application of the proposed "high-resolution" method. The steeply dipping sediment terminations against the salt are important areas for hydrocarbon exploration, and in many cases it is realistic to assume that the data close to the salt flanks do not contain energy dipping in the direction opposite to the flank reflections. The data example from the Gulf of Mexico demonstrates that the proposed method improves image resolution, without adding aliasing noise.

ACKNOWLEDGMENTS

I thank the sponsors of the Stanford Exploration Project (SEP) for supporting the research presented in this paper.

I would like to thank Unocal and Spirit Energy 76 for releasing to SEP the data set shown in the paper. In particular, I would like to thank Wook Lee, previously with Unocal, and presently with

Seislink Corporation, for preparing and sending the data.

All the reviewers of this paper (Dr. John Bancroft, Dr. Peter Cary, and Dr. Joe Dellinger) had useful comments and suggestions, which greatly helped me to improve the clarity of the exposition.

REFERENCES

Abma, R., Sun, J., and Bernitsas, N., 1998, Anti-aliasing methods in Kirchhoff migration: Geophysics, **64**, no. 6, 1783–1792.

Bevc, D., and Claerbout, J., 1992, Fast anti-aliased Kirchhoff migration and modeling: SEP–**75**, 91–96.

Biondi, B., Fomel, S., and Chemingui, N., 1998, Azimuth moveout for 3-D prestack imaging: Geophysics, **63**, no. 2, 574–588.

Brink, M., Gimse, I., Turner, P., Stolte, C., and Ronen, S., 1997, Resolution and coverage beyond traditional aliasing: 67th Ann. Internat. Meeting, Soc. Expl. Geophys., 1123–1126.

Cary, P., and Goodway, B., 1997, Migration operator aliasing and its effect on interpolation: CSEG Recorder, **10**, no. 1, 5–10.

Cary, P. W., 1997, 3D stacking of irregularly sampled data by wavefield reconstruction: 67th Ann. Internat. Meeting, Soc. Expl. Geophys., 1104–1107.

Chemingui, N., and Biondi, B., 1998, Discrete Kirchhoff theory and irregular geometry: SEP–**97**, 117–130.

Claerbout, J. F., 1995, Basic Earth Imaging: Stanford Exploration Project.

Claerbout, J. F., 1997, Geophysical exploration mapping: Environmental soundings image enhancement: Stanford Exploration Project.

Crawley, S., 1998, Shot interpolation for Radon multiple suppression: 68th Ann. Internat. Meeting, Soc. of Expl. Geophys., Expanded Abstracts, 1238–1241.

Druzhinin, A., 1999, Anti-aliased Kirchhoff-Helmholtz transformations: Geophysical Prospecting, **47**, no. 5, 757–784.

Gray, S. H., 1992, Frequency-selective design of the Kirchhoff migration operator: Geophys. Prosp., **40**, no. 5, 565–572.

Hale, D., 1991, A nonaliased integral method for dip moveout: Geophysics, **56**, no. 6, 795–805.

Lumley, D. E., Claerbout, J. F., and Bevc, D., 1994, Anti-aliased Kirchhoff 3-D migration: 64th Ann. Internat. Meeting, Soc. Expl. Geophys., 1282–1285.

Neidell, N., 1997, Perceptions in seismic imaging: The Leading Edge, **16**, no. 7,8,9,10.

Padhi, T., and Holley, T. K., 1997, Wide azimuth – why not?: The Leading Edge, **16**, 175–177.

Pica, A., 1996, Model-based anti-aliased Kirchhoff 3D PSDM: 58th Mtg. Eur. Assoc. Expl Geophys., Eur. Assoc. Expl. Geophys.

Ronen, J., 1987, Wave-equation trace interpolation: Geophysics, **52**, no. 7, 973–984.

Stolt, R. H., 1978, Migration by Fourier transform: Geophysics, **43**, no. 1, 23–48.

Wisecup, D., 1998, Unambiguous signal recovery above Nyquist using random-sample-interval imaging: Geophysics, **63**, no. 2, 763–771.

APPENDIX A

ANTI-ALIASING CONSTRAINTS FOR 3-D PRESTACK TIME MIGRATION

For 3-D prestack time migration, the reflectors' dips p_x^{I} and p_y^{I}, and the wavelet-stretch factor $dt_D/d\tau_I$, can be analytically derived as functions of the input and output trace geometry. Starting from the prestack time-migration ellipsoid (shown in Figure 19) expressed as a parametric function of the angles α and β,

$$\begin{aligned} \tau_I &= t_N \sin\alpha \cos\beta, \\ x_I &= \frac{t_D V}{2} \cos\alpha, \\ y_I &= \frac{t_N V}{2} \sin\alpha \sin\beta, \end{aligned} \tag{A-1}$$

where t_D is the time of the input impulse and t_N is the time after application of NMO. We differentiate the image coordinates with respect to the angles α and β; that is,

$$\begin{aligned} d\tau_I &= t_N (\cos\alpha \cos\beta \, d\alpha - \sin\alpha \sin\beta \, d\beta) \\ dx_I &= \frac{t_D V}{2} (-\sin\alpha \, d\alpha) \\ dy_I &= \frac{t_N V}{2} (\cos\alpha \sin\beta \, d\alpha + \sin\alpha \cos\beta \, d\beta). \end{aligned} \tag{A-2}$$

To eliminate the differentials $d\alpha$ and $d\beta$ from this set of equations, we set dy_I equal to zero when evaluating the dip p_x^{I} in the in-line direction, and set dx_I equal to zero when evaluating the dip in the cross-line direction p_y^{I}. The second step is to eliminate the angles themselves and express the image dips as a function of the image coordinates (τ_I, x_I, y_I),

$$\begin{aligned} p_x^{\mathrm{I}} &= \frac{d\tau_I}{dx_I} = \frac{2t_N}{V t_D} \frac{\cot\alpha}{\cos\beta} = \frac{4t_N^2 x_I}{V^2 t_D^2 \tau_I} \\ p_y^{\mathrm{I}} &= \frac{d\tau_I}{dy_I} = \frac{2\tan\beta}{V} = \frac{4y_I}{V^2 \tau_I}. \end{aligned} \tag{A-3}$$

The wavelet-stretch factor can be easily derived by a differentiation of the summation surfaces of 3-D prestack time migration expressed as the hyperboloids

$$t_D = t_s + t_g = \sqrt{\frac{\tau_I^2}{4} + \frac{\left|\vec{\mathbf{I}}_{\mathbf{xy}} - \vec{\mathbf{s}}\right|^2}{V^2}} + \sqrt{\frac{\tau_I^2}{4} + \frac{\left|\vec{\mathbf{I}}_{\mathbf{xy}} - \vec{\mathbf{g}}\right|^2}{V^2}}, \tag{A-4}$$

where $\vec{\mathbf{s}}$ and $\vec{\mathbf{g}}$ are the source and receiver coordinates vector, and $\vec{\mathbf{I}}_{\mathbf{xy}} = (x_I, y_I)$ represents the horizontal components of the image coordinates vector. After a few simple algebra steps, we obtain

$$\frac{dt_D}{d\tau_I} = \frac{\tau_I}{4}\left(\frac{1}{t_s} + \frac{1}{t_g}\right). \tag{A-5}$$

LIST OF FIGURES

1 3-D migrations of salt-dome flanks in the Gulf of Mexico: (a) migration obtained without the use of any anti-aliasing filter, (b) migration obtained with the application of a "standard" anti-aliasing filter.

2 A zoom into the 3-D migrations of salt-dome flanks in the Gulf of Mexico shown in Figure 1: (a) migration obtained without the use of any anti-aliasing filter, (b) migration obtained with the application of a "standard" anti-aliasing filter.

3 Data window containing aliased reflections from the salt flanks.

4 Frequency-wavenumber spectrum of the data window shown in Figure 3. Notice that the aliased events correspond to the "clouds" in the spectrum contoured with ellipses in the Figure. The ellipse marked as **B** contours the energy that can be correctly migrated. The ellipse marked as **A** contours the energy that cannot be correctly migrated and should be avoided during the summation.

5 Image obtained by constant-velocity Kirchhoff migration without the use of any anti-aliasing ($\Delta x_I = \Delta y_I = 20$ m, $V = 1.5$ km/s, and Off $= 2.4$ km). The time slice is cut at Time=1 s, and the vertical section is cut at CMP Y=1000 m.

6 Image obtained by constant-velocity Kirchhoff migration with the use of image-space anti-aliasing. ($\Delta x_I = \Delta y_I = 20$ m, $V = 1.5$ km/s, and Off $= 2.4$ km). The time slice is cut at Time=1 s, and the vertical section is cut at CMP Y=1000 m.

7 Image obtained when too strong anti-aliasing is applied because the effects of the wavelet stretch on the frequency content of the image are ignored. ($\Delta x_I = \Delta y_I = 20$ m, $V = 1.5$ km/s, and Off $= 2.4$ km). The time slice is cut at Time=1 s, and the vertical section is cut at CMP Y=1000 m.

8 Migrated section from the Gulf of Mexico salt dome: (a) $\Delta x_I = 36$ m and no anti-aliasing, (b) $\Delta x_I = 18$ m and no anti-aliasing, (c) $\Delta x_I = 18$ m and image-space anti-aliasing.

9 Two plane waves with dips of .5 s/km and -.166 s/km, 30 Hz waveform and Δx_D=25 m: a) before linear moveout, b) after linear moveout with positive dip, c) after linear moveout with negative dip. The traces on the right side of the sections are the results of stacking the corresponding data, each plane wave independently. The solid line is the stack of the positive-dip plane wave, and the dotted line is the stack of the negative-dip plane wave.

10 Two plane waves with dips of .5 s/km and -.166 s/km, 60 Hz waveform and Δx_D=25 m: a) before linear moveout, b) after linear moveout with positive dip, c) after linear moveout with negative dip. The traces on the right side of the sections are the results of stacking the corresponding data, each plane wave independently. The solid line is the stack of the positive-dip plane wave, and the dotted line is the stack of the negative-dip plane wave.

11 Two plane waves with dips of .5 s/km and -.025 s/km, 60 Hz waveform and Δx_D=25 m: a) before linear moveout, b) after linear moveout with positive dip, c) after linear moveout with negative dip. The traces on the right side of the sections are the results of stacking the corresponding data, each plane wave independently. The solid line is the stack of the positive-dip plane wave, and the dotted line is the stack of the negative-dip plane wave.

12 Graphic representation of the proposed anti-aliasing criteria [equations (4-5)]. The shaded area correspond to the "pass region". It is the widest possible area of the spectrum where there is no interference with aliased energy. On the negative wavenumber side the pass region is bound by a line that starts at -$2k_{\mathrm{Nyq}}$ and has a slope corresponding to the maximum dip $p^{\max}$. On the positive wavenumber side the pass region is bound by a line starting at $2k_{\mathrm{Nyq}}$ and with slope corresponding to the minimum dip $p^{\min}$. The dashed lines cover the areas where at least one of of the inequalities in equation (4) is satisfied.

13 Image obtained by constant-velocity Kirchhoff migration with use of "standard" anti-aliasing. ($\Delta x_I = \Delta y_I = 20$ m, $\Delta x_D = \Delta y_D = 40$ m, $V = 1.5$ km/s, and Off $= 2.4$ km). The time slice is cut

at Time=1 s, and the vertical section is cut at CMP Y=1000 m.

14 Image obtained by constant-velocity Kirchhoff migration with use of the "directed" anti-aliasing assuming $p_x^{\min} = 0$ s/m ($\Delta x_I = \Delta y_I = 20$ m, $\Delta x_D = \Delta y_D = 40$ m, $V = 1.5$ km/s, and Off $= 2.4$ km). The time slice is cut at Time=1 s, and the vertical section is cut at CMP Y=1000 m.

15 Frequency-wavenumber spectrum of a data window (same as in Figure 4). The dashed lines superimposed onto the spectrum cover the areas determined by the inequalities of equations (4-5). The areas that respect all the operator anti-aliasing constraints, and thus that represent data components used by the imaging, are covered by dashed lines along both directions.

16 3-D migrations of a salt-dome flank in the Gulf of Mexico: (a) migration obtained without any anti-aliasing filter, (b) migration obtained with the application of the proposed "high-resolution" anti-aliasing filter, (c) migration obtained with the application of a "standard" anti-aliasing filter.

17 Zoom into the shallower part of the 3-D migrations of a salt-dome flank in the Gulf of Mexico shown in Figure 16: (a) migration obtained without any anti-aliasing filter, (b) migration obtained with the application of the proposed "high-resolution" anti-aliasing filter, (c) migration obtained with the application of a "standard" anti-aliasing filter.

18 Zoom into the deeper part of the 3-D migrations of a salt-dome flank in the Gulf of Mexico shown in Figure 16: (a) migration obtained without any anti-aliasing filter, (b) migration obtained with the application of the proposed "high-resolution" anti-aliasing filter, (c) migration obtained with the application of a "standard" anti-aliasing filter.

19 Prestack time-migration ellipsoid.

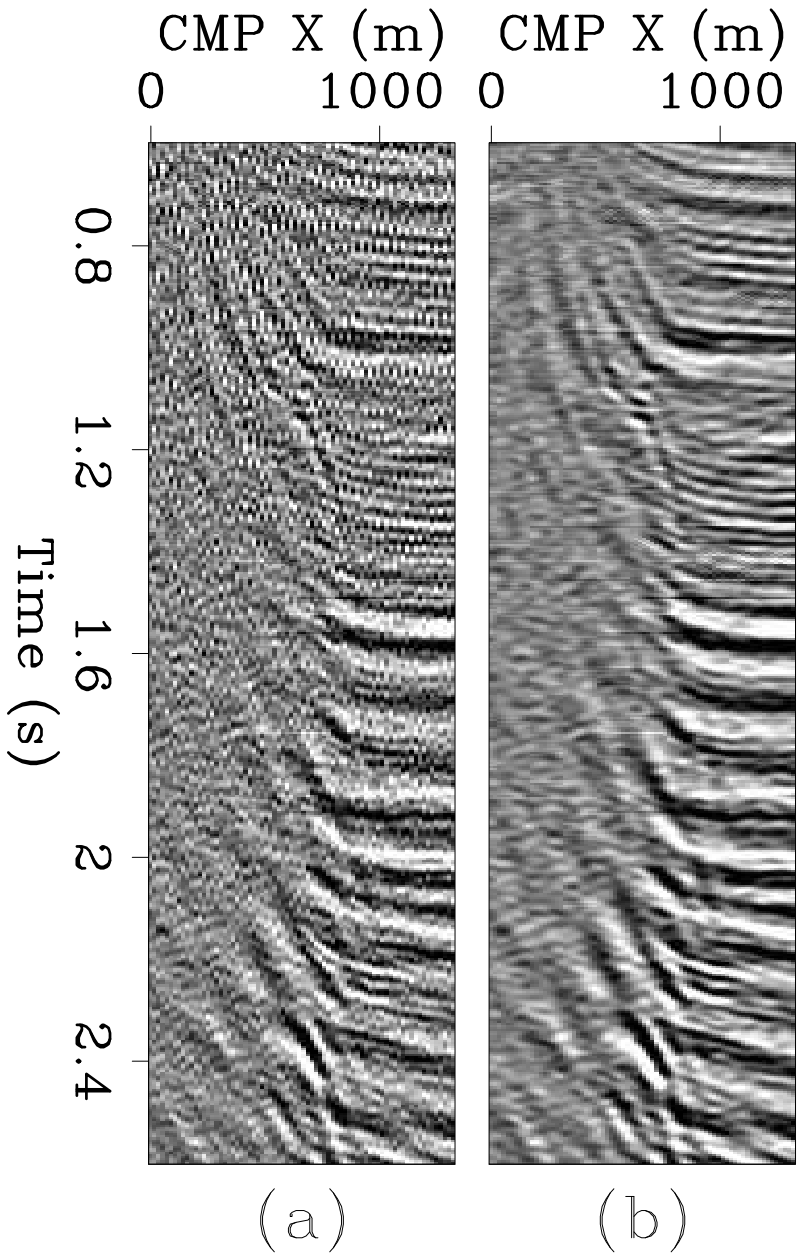

Figure 1.

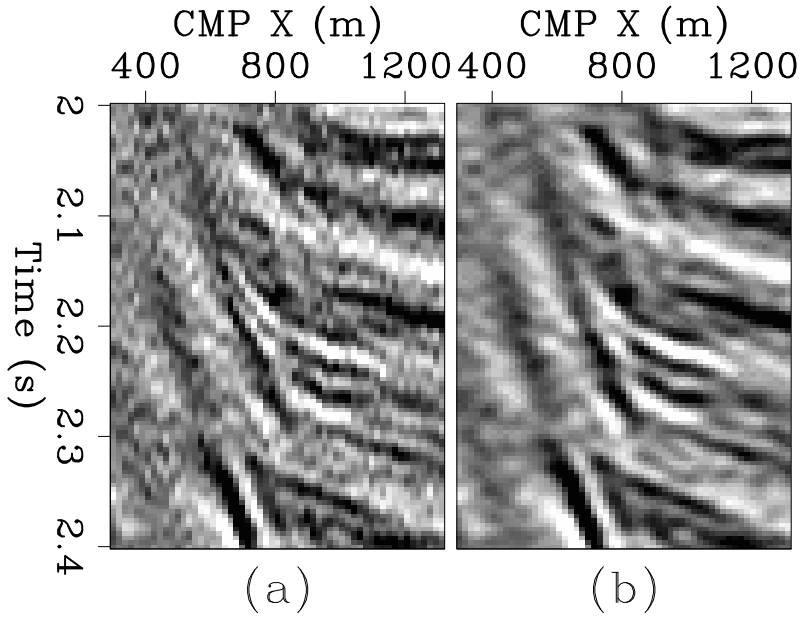

Figure 2.

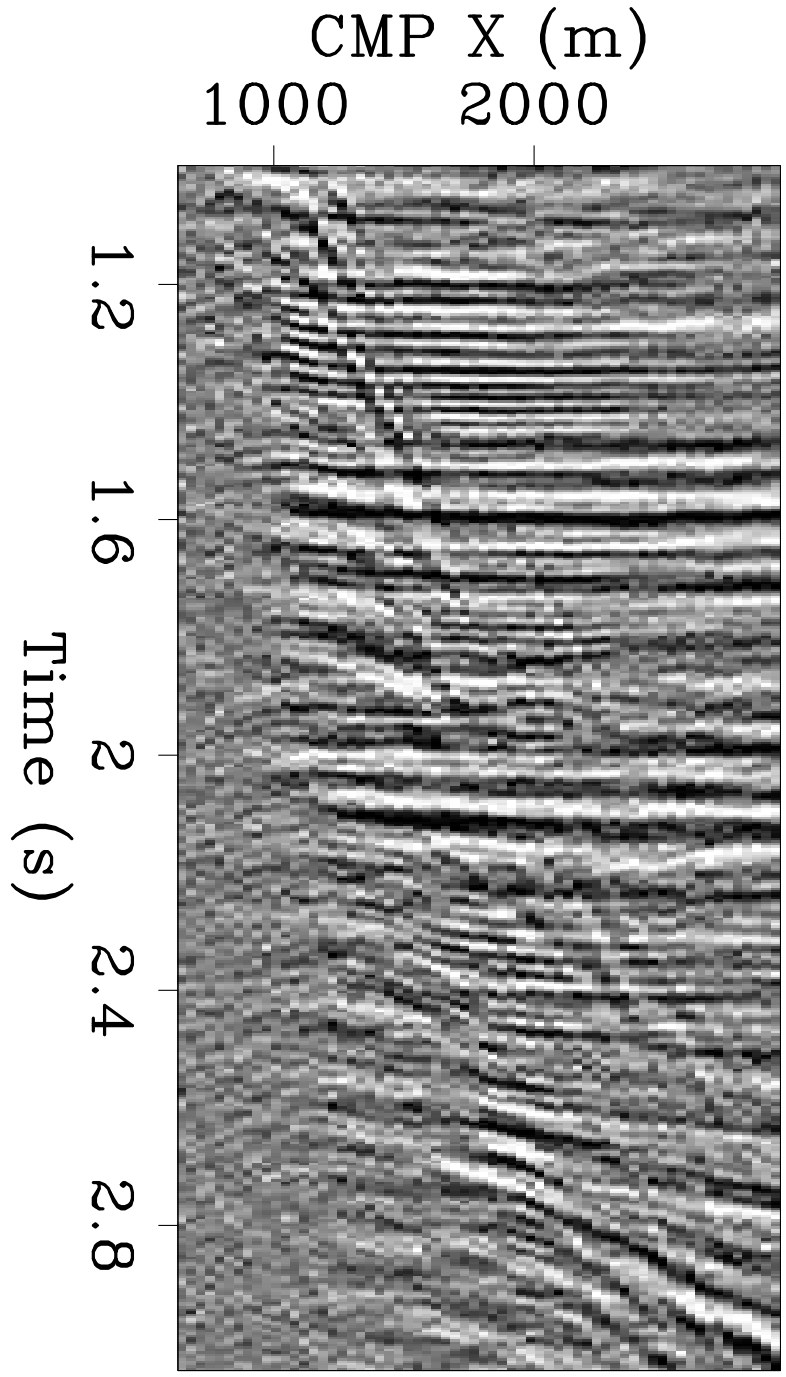

Figure 3.

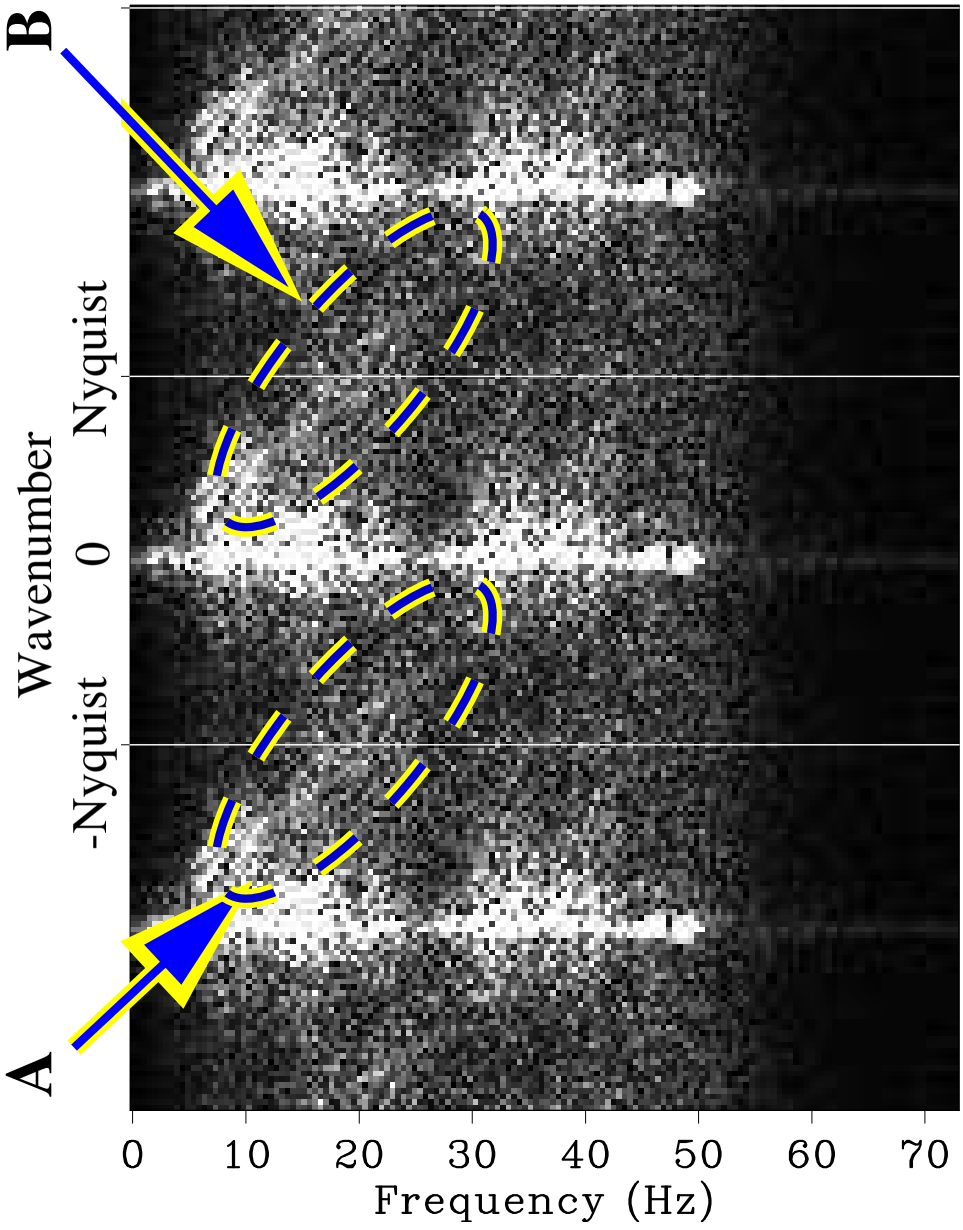
B
A
Wavenumber
Nyquist
0
-Nyquist
0
10
20
30
40
50
60
70
Frequency (Hz)

Figure 4.

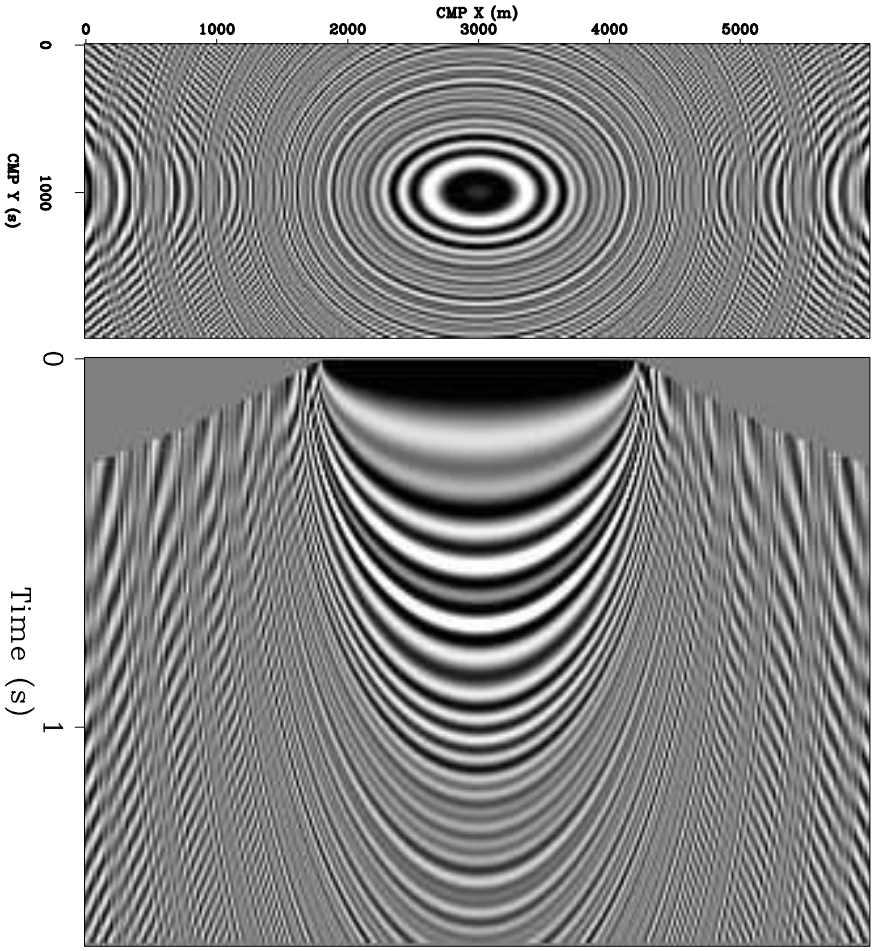

Figure 5.

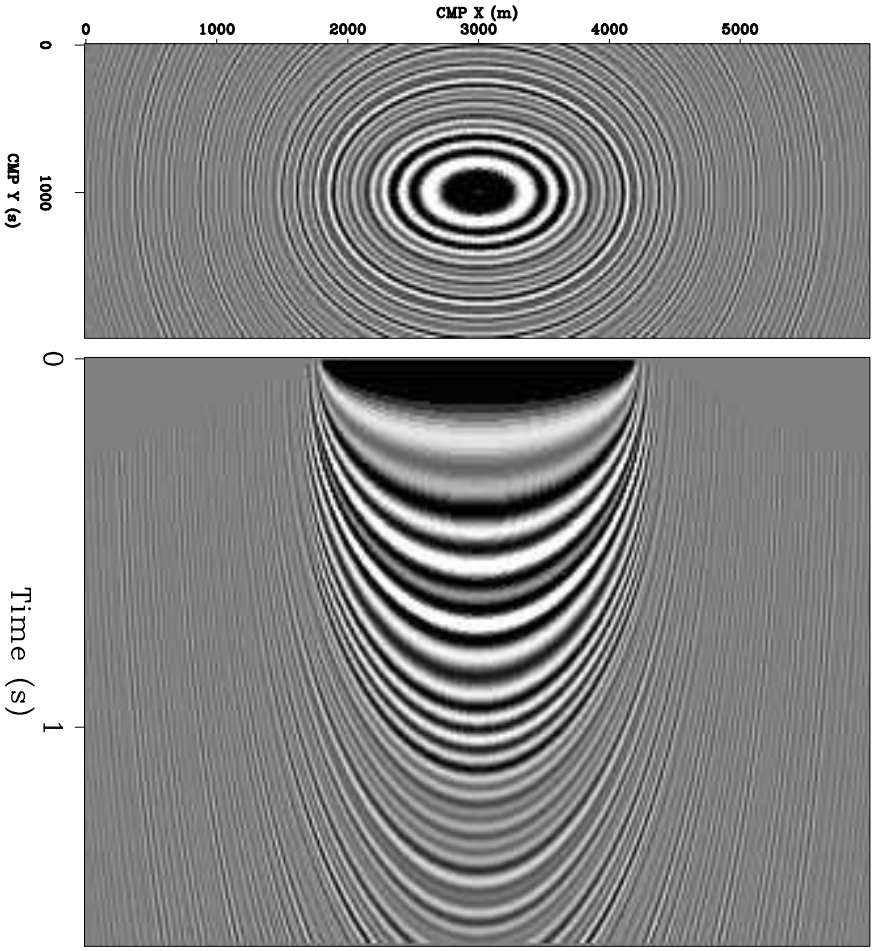

Figure 6.

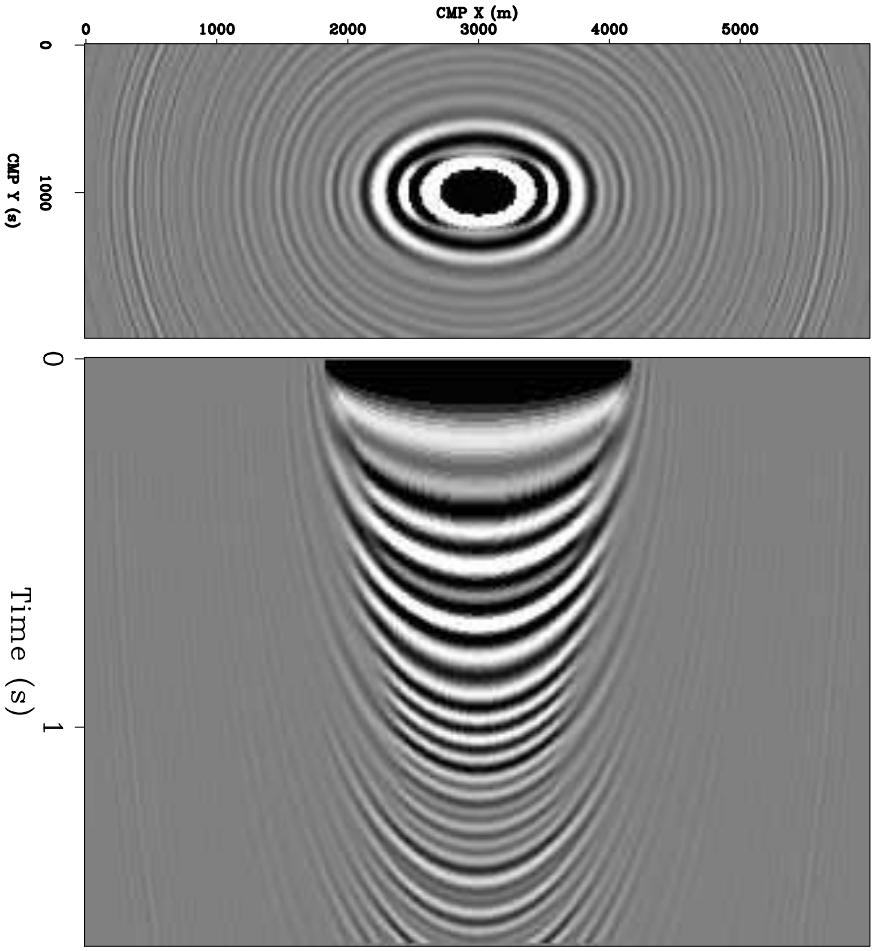

Figure 7.

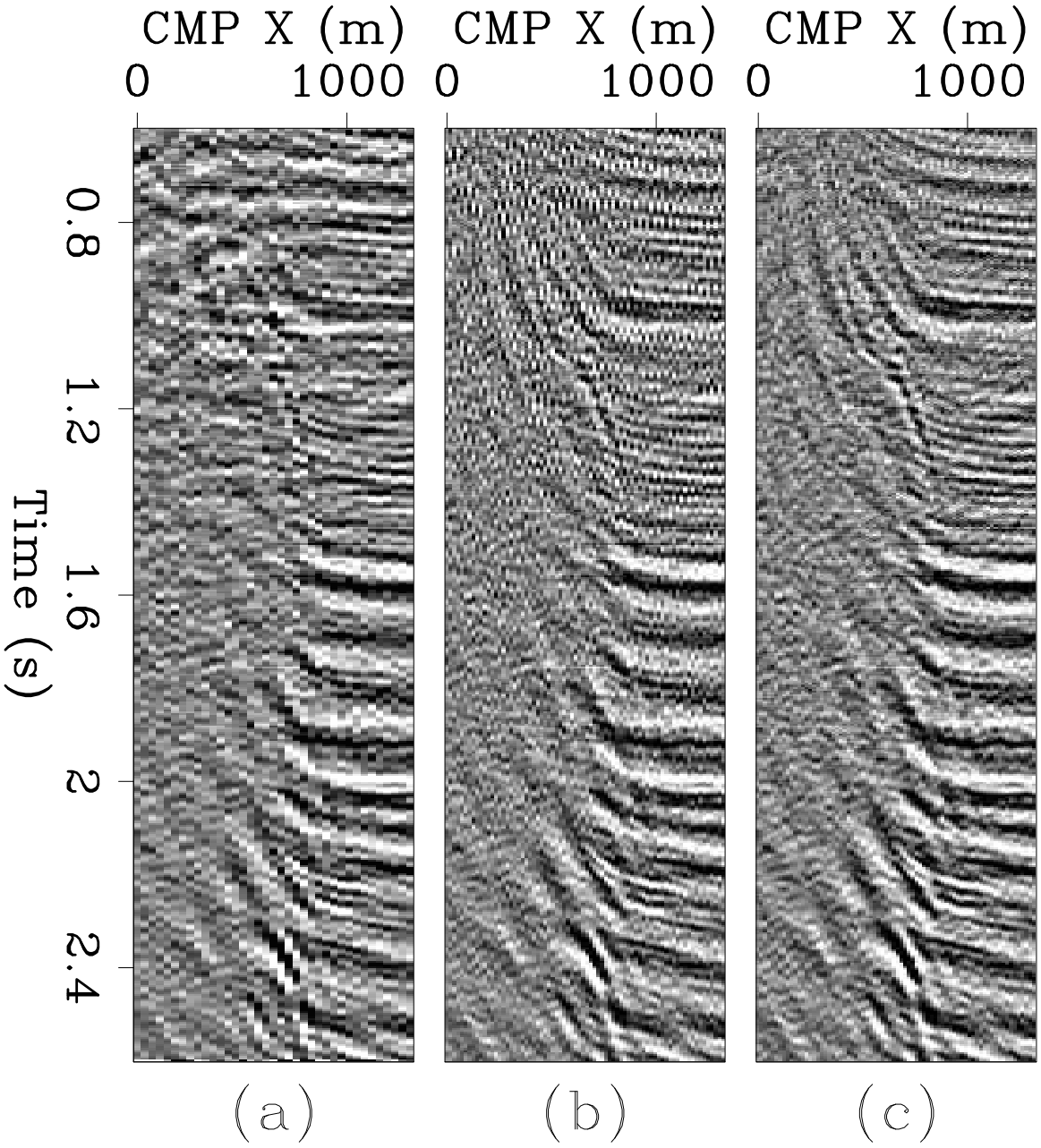

Figure 8.

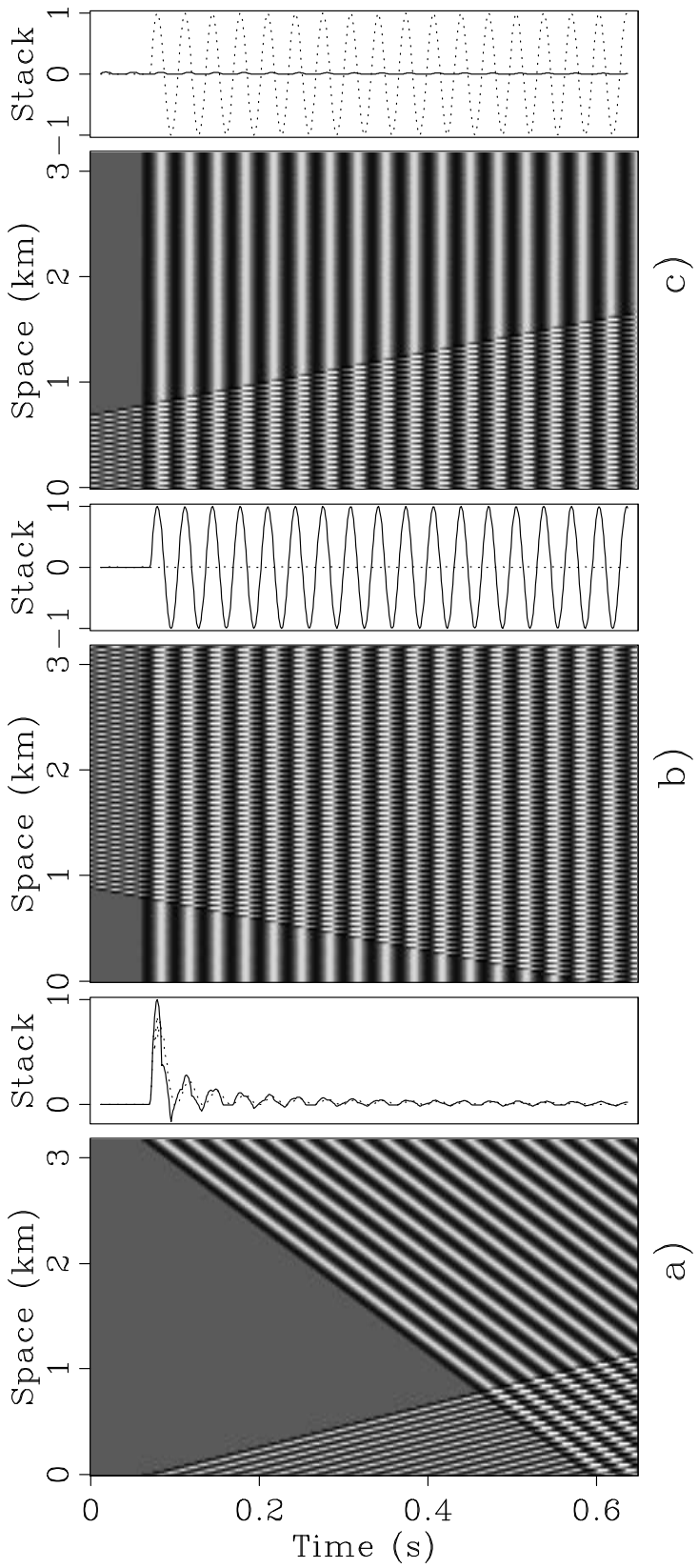
Stack
1
0
−1
3
Space (km)
2
1
10
c)
Stack
10
0
−1
3
Space (km)
2
1
10
b)
Stack
10
0
3
Space (km)
2
1
0
a)
0
0.2
0.4
0.6
Time (s)

Figure 9.

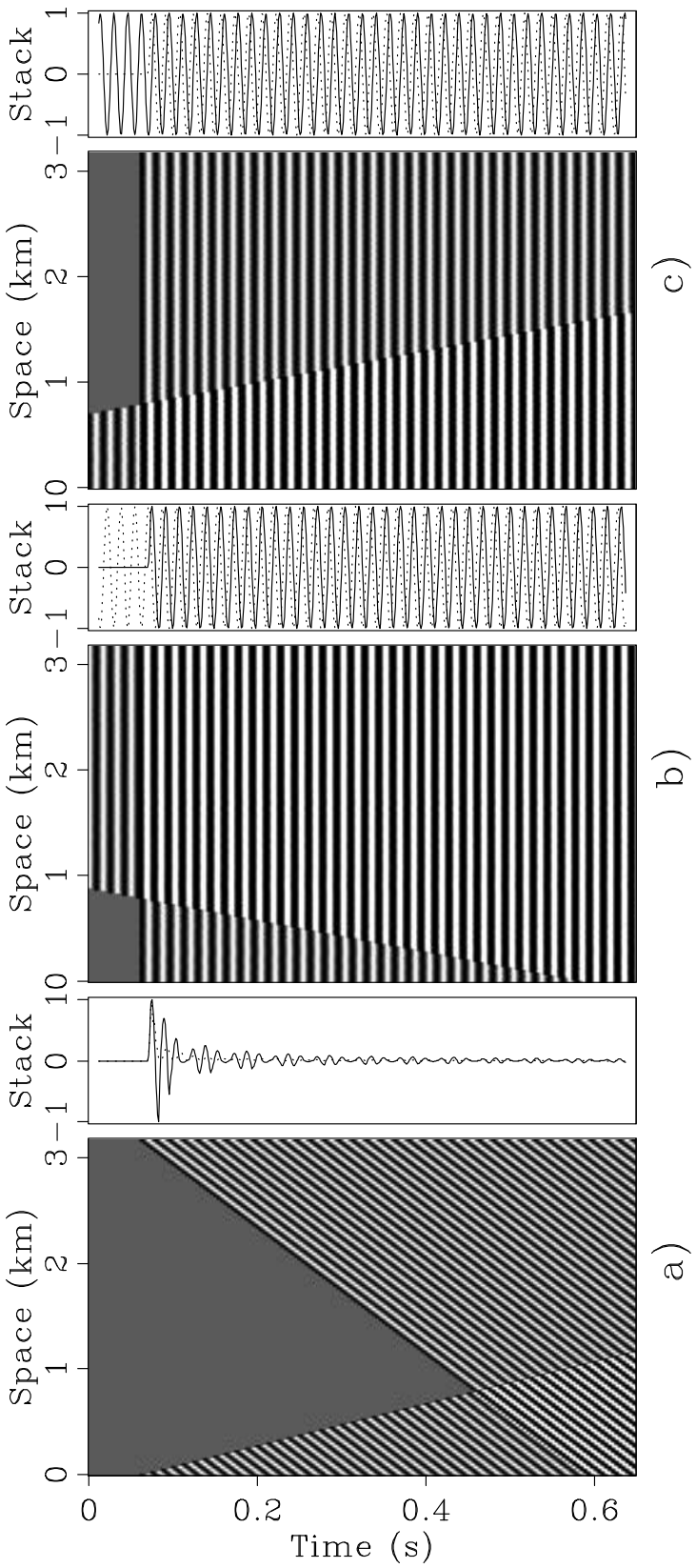

Figure 10.

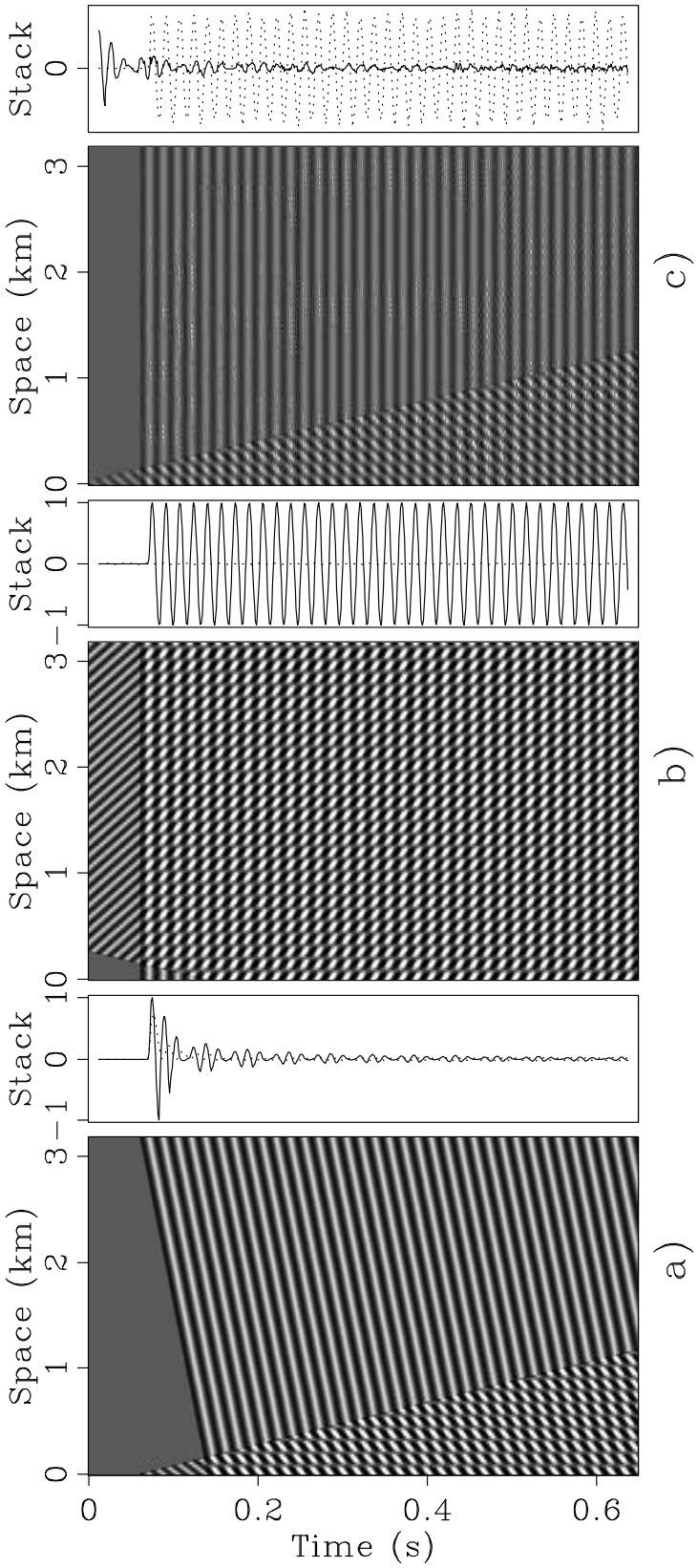

Figure 11.

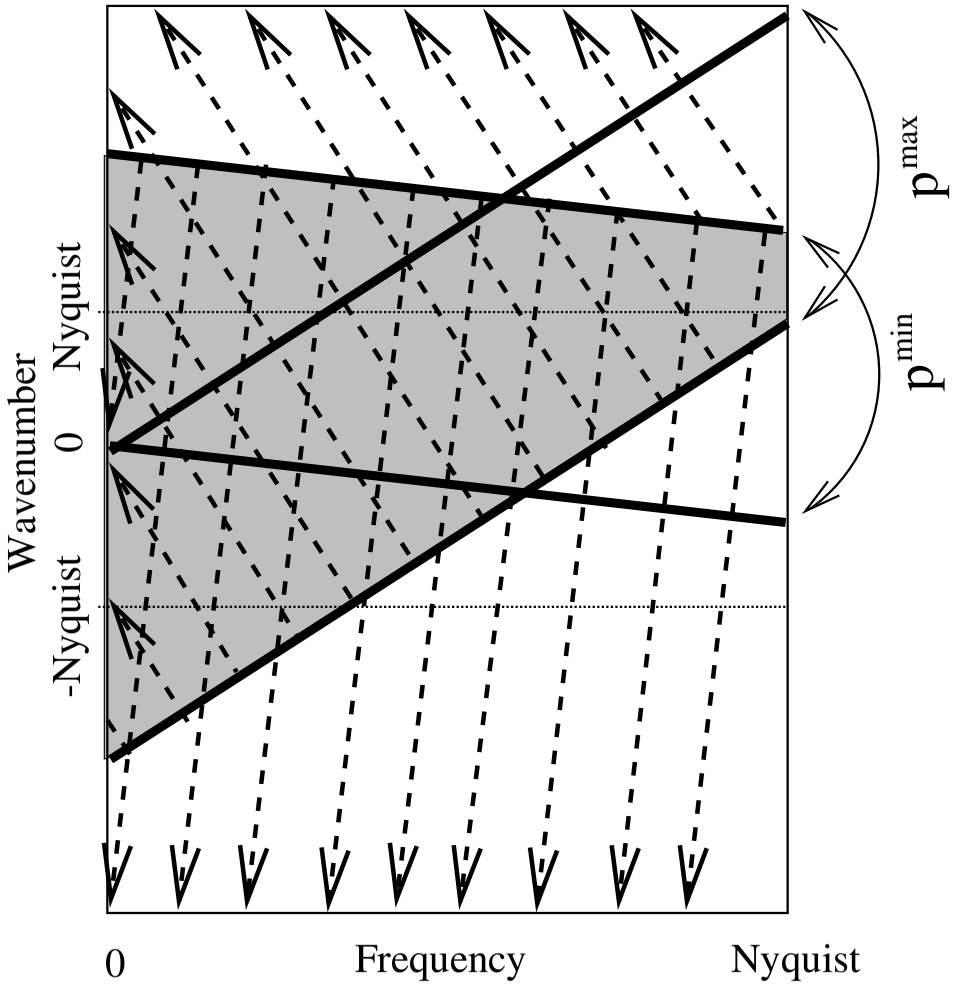
Wavenumber
Nyquist
0
-Nyquist
0
Frequency
Nyquist
p^max
p^min

Figure 12.

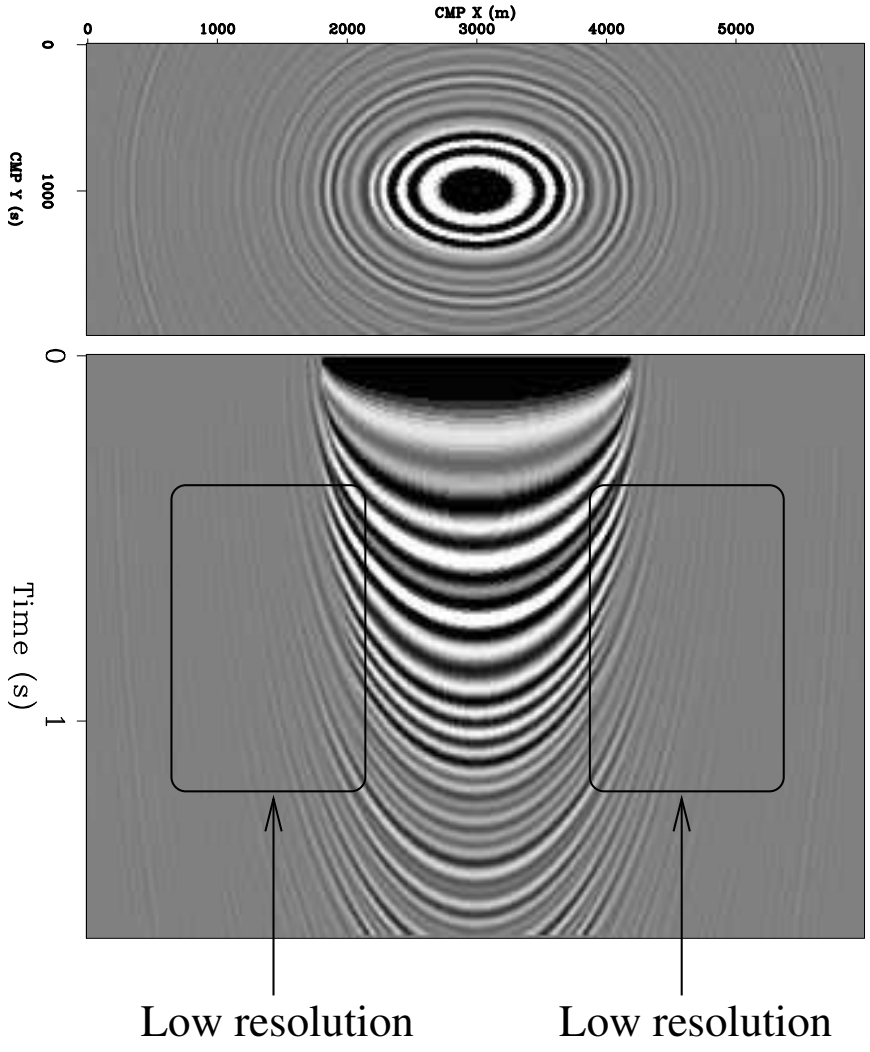
CMP X (m)
0
1000
2000
3000
4000
5000
0
1000
CMP Y (s)
0
1
Time (s)
Low resolution
Low resolution

Figure 13.

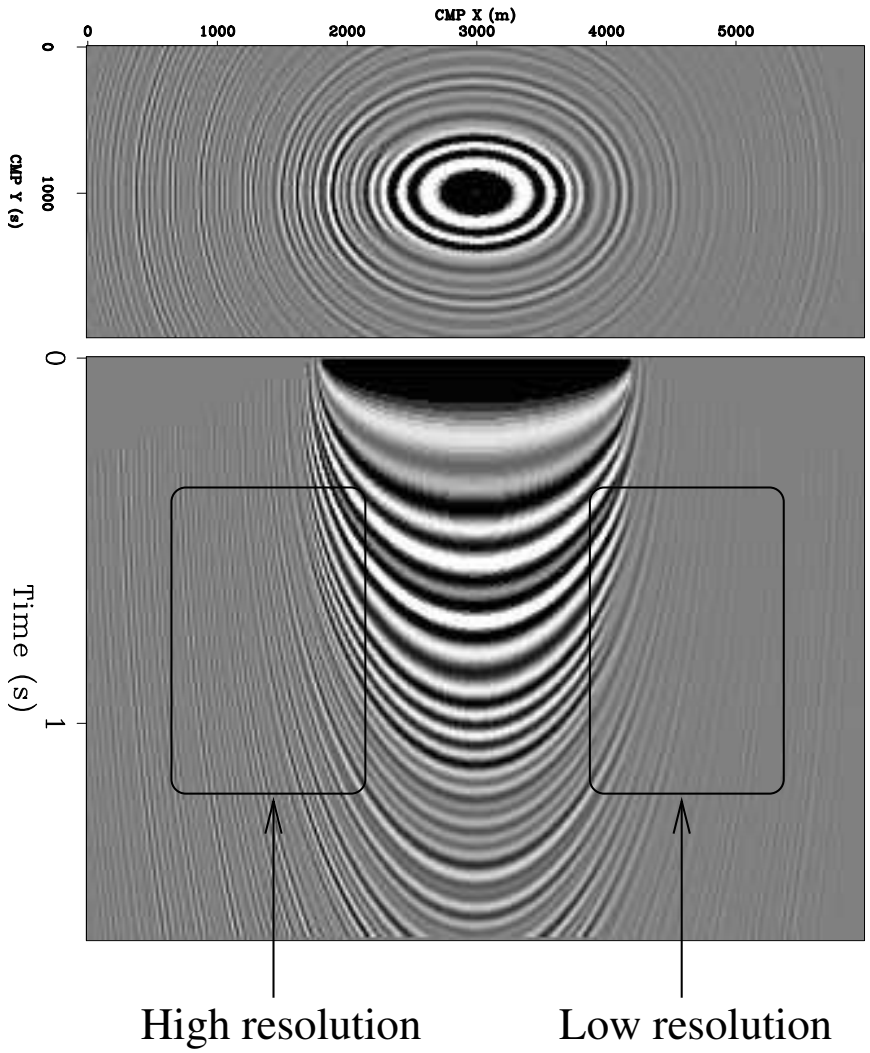
CMP X (m)
0
1000
2000
3000
4000
5000
CMP Y (s)
0
1000
Time (s)
0
1
High resolution
Low resolution

Figure 14.

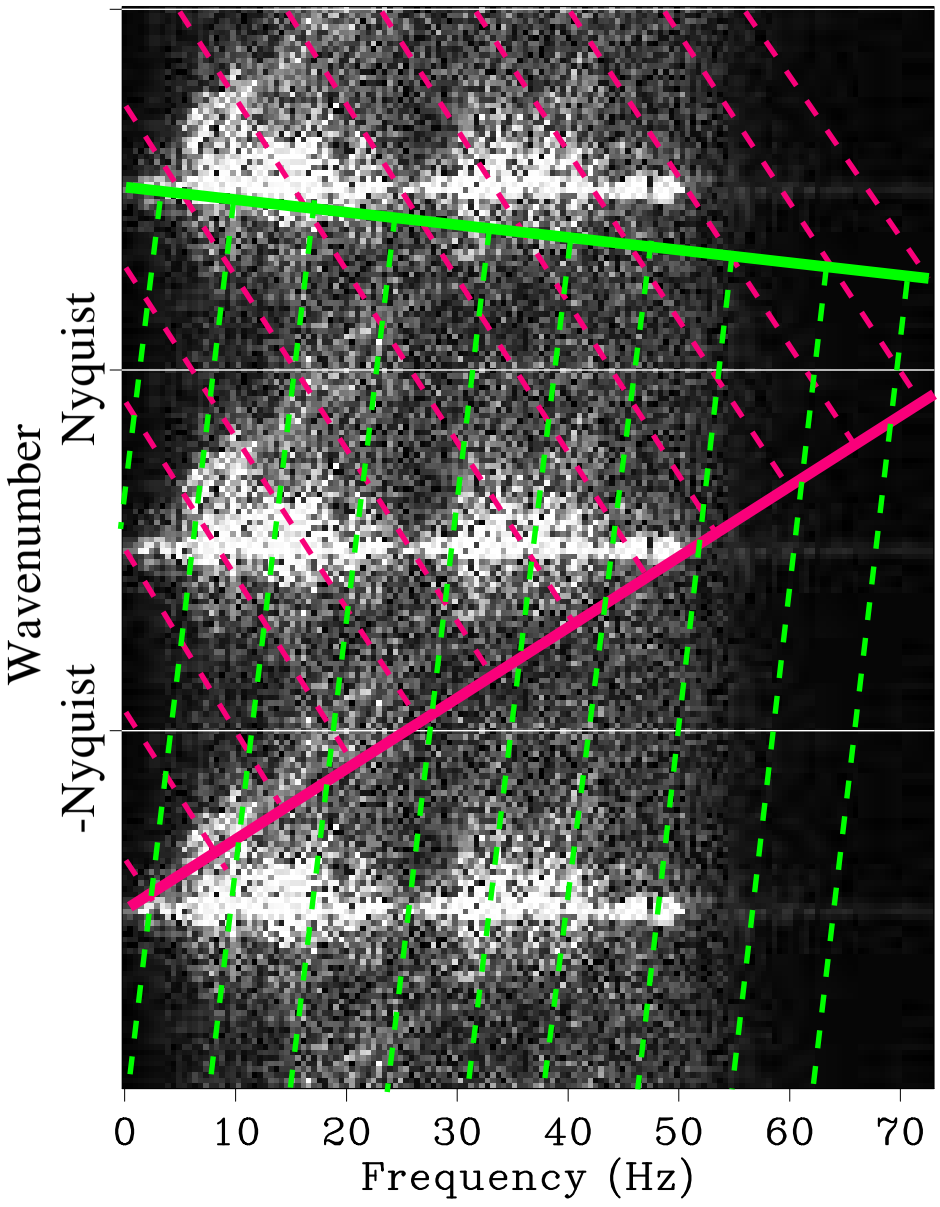
Wavenumber
Nyquist
-Nyquist
0
10
20
30
40
50
60
70
Frequency (Hz)

Figure 15.

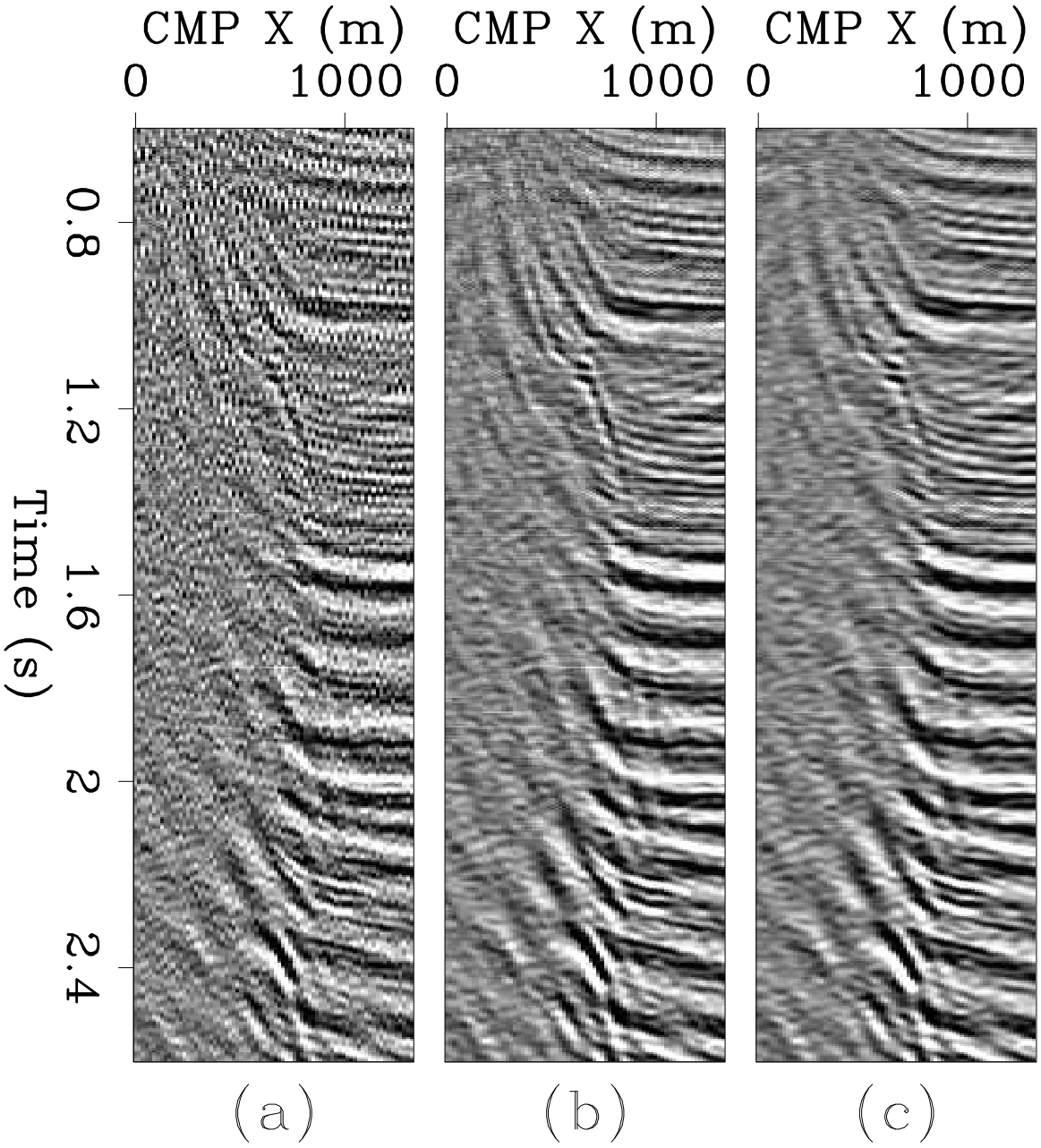

Figure 16.

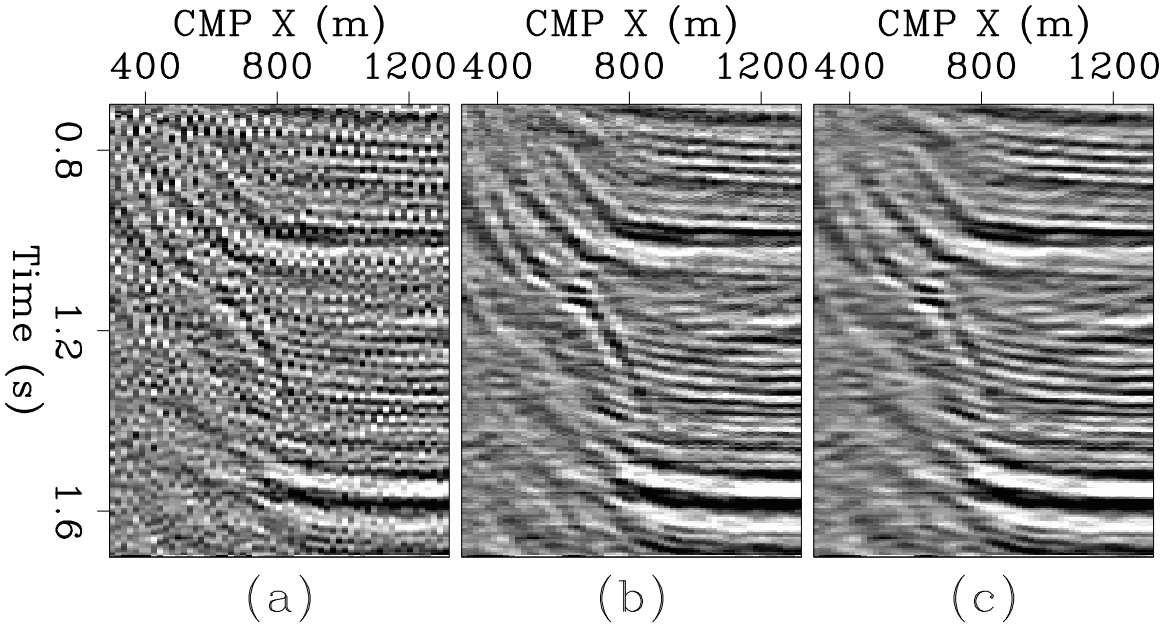
CMP X (m)
400
800
1200
CMP X (m)
400
800
1200
CMP X (m)
400
800
1200
Time (s)
0.8
1.2
1.6
(a)
(b)
(c)

Figure 17.

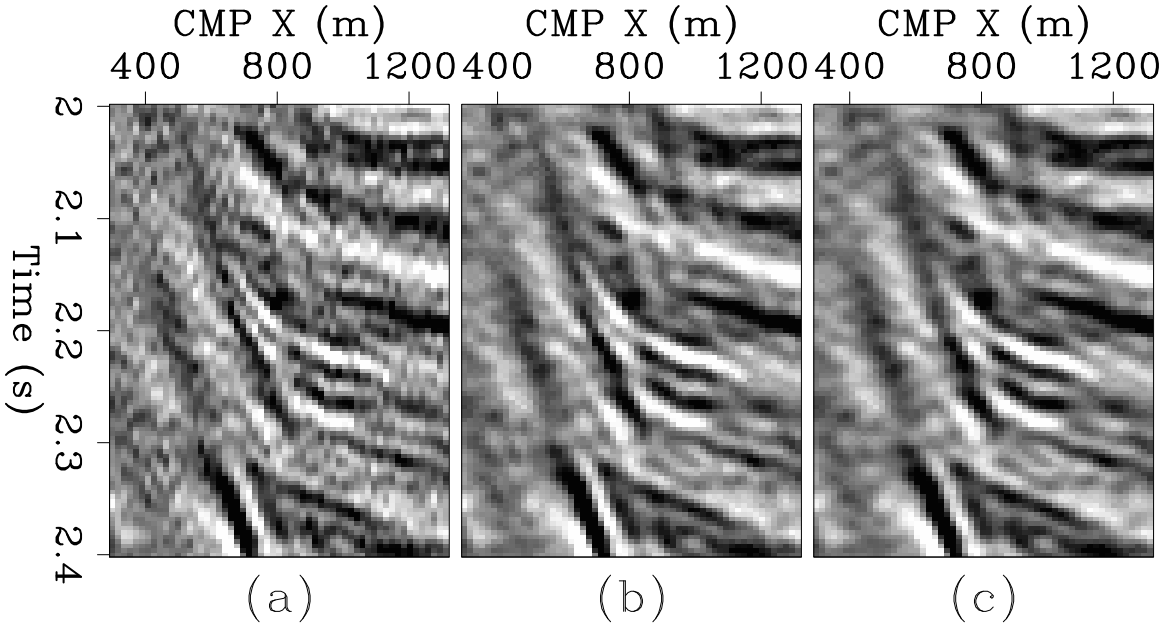
CMP X (m)
400
800
1200
CMP X (m)
400
800
1200
CMP X (m)
400
800
1200
Time (s)
2
2.1
2.2
2.3
2.4
(a)
(b)
(c)

Figure 18.

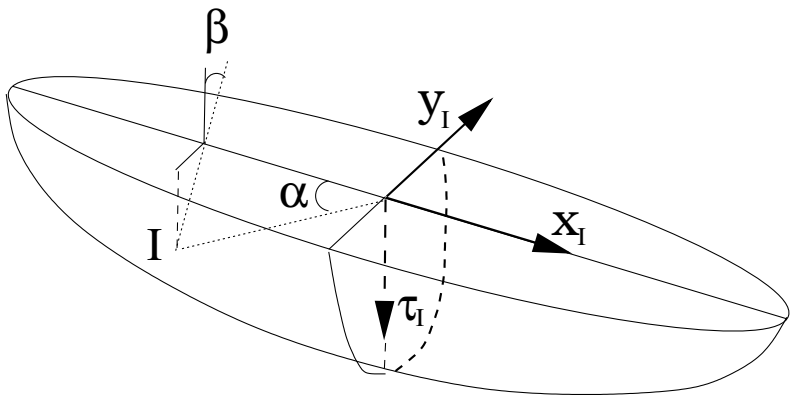

Figure 19.